Navier-Stokes Solution for a Complete Re-Entry Configuration

J. S. Shang* and S. J. Scherr†
Air Force Wright Aeronautical Laboratories, Wright-Patterson Air Force Base, Ohio

This article represents a first attempt at numerical simulation of the flowfield around a complete lifting body configuration utilizing the Reynolds-averaged Navier-Stokes equations. The numerical solution generated for the experimental aircraft concept X24C-10D, at a Mach number of 5.95, exhibited accurate prediction of detailed flow properties and integrated areodynamic coefficients as well. In addition, the present analysis demonstrated that a vectorized processor with an external memory device is an efficient and viable means for processing the Navier-Stokes equations.

Nomenclature

A = reference area for aerodynamic force coefficient $= 1303.2$ cm^2
C_D = drag coefficient $= 2D/\rho_\infty U_\infty^2 A$
C_L = lift coefficient $= 2L/\rho_\infty U_\infty^2 A$
C_p = specific heat at constant pressure
e = specific internal energy $= C_v T + 0.5(u^2+v^2+w^2)$
F,G,H = flux vectors of conservation equations
H_∞ = stagnation enthalpy of the freestream
h = enthalpy
$\bar{\bar{I}}$ = identity matrix
$\hat{i},\hat{j},\hat{k}$ = unit vectors in Cartesian frame
M = Mach number
$\bar{n}$ = surface outward normal
p = static pressure
Pr = molecular Prandtl number
Pr_t = turbulent Prandtl number
q = rate of heat transfer; $\bar{q} = -k\nabla T$
r_N = radius of the blunt nose $= 0.4826$ cm
Rey = Reynolds number
St = Stanton number, Eq. (12)
t = time
T = temperature
u,v,w = velocity components in the Cartesian frame
U = dependent variables $= U(\rho,\rho u,\rho v,\rho w,\rho e)$
x,y,z = coordinates of the Cartesian frame
γ = ratio of specific heats
ϵ = eddy-viscosity coefficient
μ = molecular viscosity coefficient
ξ,η,ζ = transformed coefficient
ρ = density
$\bar{\bar{\tau}}$ = stress sensor

Subscripts

w = surface condition
0 = stagnation condition
∞ = freestream condition

Superscript

T = transpose of

Introduction

A CONTINUAL and systematic progression of path-finding research in solving the Navier-Stokes equations has paved the way for the first attempt to numerically simulate the flowfield around a complete lifting body configuration.[1-4] In the present investigation, a hypersonic research aircraft, the X24C-10D, is selected for its rather complex blunt leading edges, canopy, strake, fin, and wing formations, which are typical of those encountered in a modern aerospace vehicle (Fig. 1). For the chosen aircraft, a detailed experimental data base also exists in the form of a flowfield pitot survey, surface pressure, heat transfer, and force and moment measurements.[5-7] This experimental data establishes a solid criterion for assessment of the accuracy of the simulation.

In principle, a composite solution using varying degrees of simplification of the Reynolds-averaged Navier-Stokes equations for the flowfield around a complete aircraft is possible. However, prior knowledge or unique insight into the flowfield[8-10] structure is required to implement this zonal approach. As a benchmark calculation, the uncertainty is removed by seeking a solution of the Reynolds-averaged Navier-Stokes equations. In order to depict adequately the investigated aircraft configuration, a mesh system of 475,200 nodes was adopted. At present, processing and managing this huge amount of data requires a very large-scale vector processor with an external storage device. In essence, the adaptation of a numerical procedure to a very large-scale computer comprises construction of a data base according to the computer architecture, and implementation of the procedure to minimize data movement.[1,3] This is the first consideration so that one can extract the maximum data processing efficiency from a vector processor.

Since there are no sharp leading edges in the configuration investigated, a composite grid system specially designed for high local numerical resolution is unnecessary.[4] A single surface clustered body-conformal grid system is sufficient to facilitate the aerodynamic force calculations. The adopted MacCormack explicit, unsplit algorithm[11] is known to advance in time with the minimum number of data accesses and has attained extremely high vector efficiency by continual improvement.[1,3] Most important, the stencil of this algorithm requires no more than four contiguous nodes to be processed simultaneously in any given coordinate. This

Presented as Paper 85-1509 at the AIAA 7th Computational Fluid Dynamics Conference, Cincinnati, OH, July 16-18, 1985; received Sept. 26, 1985; revision received Feb. 11, 1986.

*Technical Manager, Computational Aerodynamics Group. Associate Fellow AIAA.
†Mathematician. Member AIAA.

feature leads naturally to a page structure in grid-point-system construction, and eliminates the need for interface boundary conditions or repetitious regrouping of data to accomplish a particular orientation for a numerical sweep.[12]

The numerical simulation was performed for the flowfield around the entire aircraft at 6-deg angle of attack with a nominal Mach number of 5.95 and the characteristic Reynolds number of 16.4×10^6/m. The benchmark numerical results will first be evaluated for accuracy in practical applications by prediction of the surface pressure distributions, shock-wave structure, heat transfer, surface shear-stress pattern, and the integrated aerodynamic force coefficients whenever comparison data are available. The overall numerical procedure is assessed for its relative efficiency, practical application value, and the areas of emphasis for future aerodynamics research.

Governing Equations

The three-dimensional, compressible, Reynolds-averaged Navier-Stokes equations in chain-rule conservation form are given as[1]

$$\frac{\partial U}{\partial t}+(\xi_x,\xi_y,\xi_z)\left(\frac{\partial F}{\partial\xi},\frac{\partial G}{\partial\xi},\frac{\partial H}{\partial\xi}\right)^T+(\eta_x,\eta_y,\eta_z)\times\left(\frac{\partial F}{\partial\eta},\frac{\partial G}{\partial\eta},\frac{\partial H}{\partial\eta}\right)^T(\zeta_x,\zeta_y,\zeta_z)\left(\frac{\partial F}{\partial\zeta},\frac{\partial G}{\partial\zeta},\frac{\partial H}{\partial\zeta}\right)^T=0 \tag{1}$$

It is easily identifiable that the dependent variable U consists of ρ, $\rho\bar{u}$, and ρe

$$U=U(\rho,\rho u,\rho v,\rho w,\rho e) \tag{2}$$

The flux vectors, F, G, and H, are simply the components of vectorial quantities of the continuity and energy equations, as well as the tensorial quantities of the momentum equations contained within the divergence operator of the conservation law.[1]

The closure of this system of equations is obtained by including the Baldwin-Lomax turbulence model[13] for the stress tensor and by assigning a turbulent Prandtl number with a value of 0.9 for the heat flux,

$$\bar{\bar{\tau}}=-\left[p+\frac{2}{3}(\mu+\epsilon)\nabla\cdot\bar{u}\right]\bar{\bar{I}}+(\mu+\epsilon)\ \mathrm{def}\bar{u} \tag{3}$$

$$\bar{q}=-\left(\frac{C_p\mu}{Pr}+\frac{C_p\epsilon}{Pr_t}\right)\nabla T \tag{4}$$

as well as the equation of state for a perfect gas, and Sutherland's formula for the molecular viscosity coefficient. The description of this differential system of equations is complete once the appropriate and well-posed initial and boundary conditions are specified.

In the present analysis we have taken advantage of the no-yaw flight condition, requiring that only one-half of the configuration be computed with respect to the plane of symmetry. This simplification, applied together with the idea of analytic continuation, results in the leading coordinate surface ($\xi=0$) at the blunt nose becoming a developable surface by reflection. In this manner, the adopted grid system is body conformal and simply connected, and the entire computational domain can be mapped into a unit cube. Details of the construction of the mesh system, including the topology definition and the grid-generation procedure, may be found in an accompanying paper.[14] In the transformed space, the initial and boundary conditions are summarized as follows.

Initial and boundary conditions:

$$U(0,\xi,\eta,\zeta)=U_\infty \tag{5}$$

The $\xi=0$ surface is purely a numerical boundary created by the grid system. Since the two initial data pages in ξ are mirror images, the boundary values will be updated automatically. The $\xi=1$ surface represents the downstream boundary. The extrapolation condition commonly used is

$$\left.\frac{\partial U}{\partial\xi}\right|_{\xi=1}=0 \tag{6}$$

On the body surface, $\eta=0$, the no-slip condition for velocity components and the surface temperature duplicating the experimental condition are given. The value of density on the solid contour is derived from the isobaric condition normal to the surface.

$$u=v=w=0 \tag{7}$$

$$T_w=316.7\ \mathrm{K} \tag{8}$$

and

$$\bar{n}\cdot\nabla p=0 \tag{9}$$

where $\bar{n}$ is the $\eta=0$ surface outward normal

$$\bar{n}=\frac{\eta_x\hat{i}+\eta_y\hat{j}+\eta_z\hat{k}}{\sqrt{\eta_x^2+\eta_y^2+\eta_z^2}}$$

$\hat{i}$, $\hat{j}$, $\hat{k}$ denote the unit vectors in the fundamental Cartesian frame. The far-field boundary has transformed into the $\eta=1$ surface. This boundary is located outside the enveloping bow-shock-wave system, where the flow retains the unperturbed freestream value

$$U=U_\infty \tag{10}$$

Surfaces $\zeta=0$ and 1 lay across the plane of symmetry. The following condition of symmetry prevails

$$\frac{\partial U}{\partial\zeta}=0,\quad w=0 \tag{11}$$

Numerical Procedure

All calculations were performed on a vector processor with an eight-million-word MOS memory unit, the Solid-State Storage Device (SSD). A mesh system consisting of 475,200 nodes was utilized to depict the complete aircraft configuration. Specificially, 110 nodes were assigned to define the cross section of the aircraft in 120 streamwise stations. Thirty-six nodes were used to accommodate the computational domain bounded by the solid contours and far field.

MacCormack's explicit, unsplit algorithm vectorizes easily with ample opportunities for chaining operations. This reliable, conditionally stable scheme, when incorporated with a time-warp acceleration procedure, has demonstrated efficiency gains of a factor of 6 or more for solutions that possess a steady-state asymptote.[1,15] The coordinate transformation derivatives are repeatedly generated by a three-point, second-order differencing scheme as needed without allocating a permanent storage space. Those additional arithmetic operations substantially reduce memory requirements but yield an in-core data processing rate of 3.077×10^{-5} s/iteration/node point.

In essence, computation of the three-dimensional, Reynolds-averaged Navier-Stokes equations becomes a data-transfer-intensive procedure between the central processor unit (CPU) and the data storage device (SSD). In the present

investigation, 120 streamwise stations were divided into 20 data blocks of six pages each. The minimum bandwidth that can support the four-page data base is the six-page block. The additional two pages provide the coordinate transformation derivatives at the four-page data interfaces. Each block of data was assigned a data set of 213,840 words. Two blocks, or 12 pages of data, were resident in the CPU during the numerical sweep between the upstream and downstream boundaries. A measure of the relative efficiency for adaptation of a numerical procedure to a very large computer with an external memory device is the degradation of the data processing rate (DPR) in comparison with in-core performance. For the present investigation, where a total of 4,276,800 words is processed by a 800,000-word CPU, the degradation is less than 23% in DPR. The data processing rate in conjunction with the SSD is consistently 3.7814×10^{-5} s/iteration/grid point.

As a pleasant surprise, the page and block data structure has been demonstrated to reduce the required computing time for overall convergence. Due to the numerical sweep bias, the upstream section tends to converge sooner than the downstream section. Then, it no longer needs to be rotated into the CPU, and the total number of data blocks can be truncated accordingly. A net saving in computing time of up to 30% has been realized by suppressing unnecessary calculation in the converged region. Computation performed for this truncated domain is effectively equivalent to a zonal method, but has no need of explicit zonal boundary conditions.

For the numerical simulation of a complete aircraft, the surface normal grid spacing required to resolve the shear stress or heat transfer can no longer be gaged by a single selected value of the law-of-the-wall variable, y^+. Consideration must be given to the large upstream ratio between normal and peripheral mesh sizes and the growth rate of the boundary layer along the entire configuration. From two different estimates of the laminar sublayer thickness based upon a turbulent boundary-layer scaling law, the minimum surface normal step size was determined to be 9.1×10^{-3} cm ($y^+ = 9.2$). This nominal value was used as a guide to set an appropriate overall grid spacing and a finer mesh size in the nose region, where the surface normal step size is a factor 4.09 times finer than the nominal value. The peripheral node distribution is weighted by the local radius of curvature. In the streamwise direction, the ratio between the maximum and minimum step size is as high as 19.47. The high grid density zones were concentrated around the nose region and the locations where the canopy, strake, and fin protrude into the oncoming stream (see Fig. 1). Analysis of the flowfield immediately downstream of the blunt nose through the emergence of the strake by a parabolized Navier-Stokes scheme[8,9] indicated that the maximum grid spacing could be used in this region. The assigned value was 1.448 cm. Finally, the steady asymptote of the numerical solution is considered to be reached when the L_2 norm between two consecutive normalized pressure values is less than 10^{-5}. This criterion is much less stringent than the evaluation of heat transfer and is considered suitable for our purpose.

Discussion of Numerical Results

Since most of the experimental data was collected at several predetermined streamwise stations, the format of comparison is constructed accordingly. Typical results are given by abscissas in the form of the normalized arc length. This length is computed from the leeward meridional plane toward the windward counterpart and scaled by the total arc length of each individual cross section. In Figs. 2 and 3, a total of 11 streamwise stations are depicted. These stations represent a sequential evolution from the blunt-nose region to the trailing section. The physical locations span a range of 15 to 141.25 radii from the coordinate origin, which is 3.35

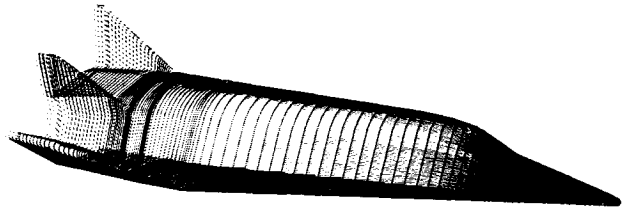

Fig. 1 X24C-10D configuration.

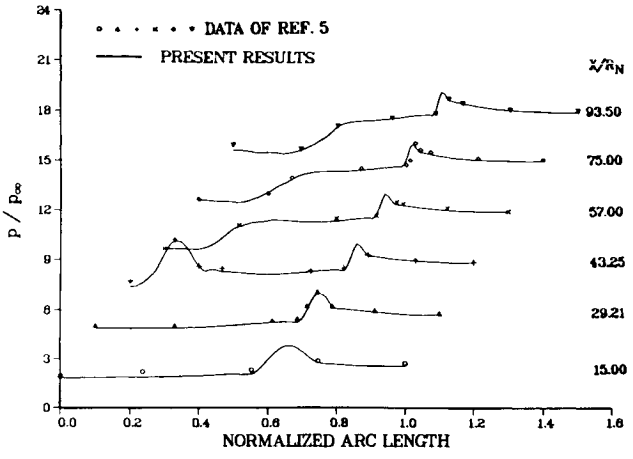

Fig. 2 Peripheral surface pressure distributions of the forebody.

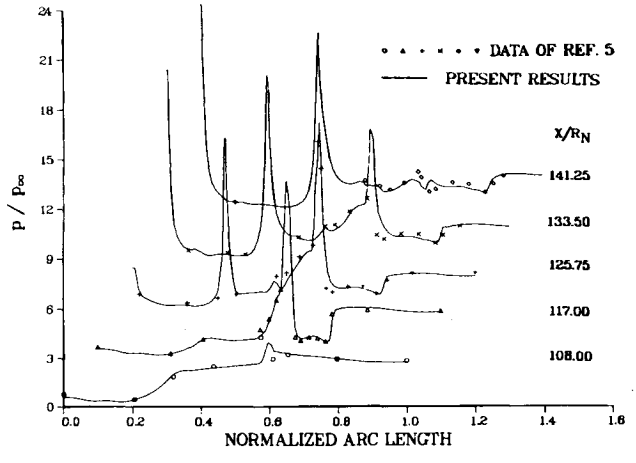

Fig. 3 Peripheral surface distributions of the afterbody.

radii upstream of the blunt nose, $r_N = 0.483$ cm. The overall agreement between data and numerical results is excellent. In Fig. 2, the streamwise compression and its subsequent expansion around the canopy due to the recessed and flattened out leeward surface are obvious. In each cross-sectional plane, the expansion from windward to leeward domains stands out. The surface pressure distributions also exhibit a relatively mild compression at the lower corner of the trapezoidal cross section. This local phenomenon bears a strong resemblance to that of the blunt leading edge of a delta wing.[16] The surface pressure distributions of the afterbody are given in Fig. 3. Each pressure spike represents the result of protruding fins or strake into the oncoming stream. The pressure distribution reveals the emergence of the central fin near the origin of the abscissas, the middle fin, and the strake from the afterbody. Finally, the strake, due to recession, ceases to be an exposed blunt edge ($x/r = 141.25$). Unfortunately, the $x/r = 125.75$ station has only two pressure taps installed on the leading edge of the strake. Nevertheless,

the agreement between the data and the numerical results is excellent.

Three pressure distributions around the central fin at different elevations ($z/r=20$, 25, 30) are given in Fig. 4. These elevations correspond to distances of 0.92, 3.33, and 5.74 cm above the upper model surface.[5] The collapsing of all pressure distributions into a narrow band reveals that, in spite of all upstream disturbances, the leeward flowfield immediately surrounding the central fin remains nearly uniform at this moderate angle of attack. The maximum deviation between data and calculations is limited to a few percent.

The flowfield survey data by pitot pressure probes[6] is presented together with the computed impact pressure contour in Fig. 5. It is clearly exhibited that the numerical simulation duplicates the measurements. The definition of the shock-wave system as captured by the numerical mean is comparable to the data-scattering band.[6] As mentioned earlier, the enveloping shock-wave system has attenuated substantially in the leeward region to be detected as a Mach wave.

Figure 6 depicts the heat transfer in the form of Stanton number distributions in five streamwise stations ($x/r=108$, 117, 125.75, 133.50, 141.25). These data-collecting stations are identical to those of the surface pressure in the afterbody region. The Stanton number is defined as

$$St = |\dot{q}|/\rho_\infty u_\infty (H_\infty - h_w) \tag{12}$$

The numerical value of the rate of heat transfer was computed directly from the profiles of specific internal energy instead of static temperature to take advantage of the monotonic distribution of the former adjacent to the body surface. The specific formula used is

$$St = \frac{\gamma \mu_w}{Pr}(\eta_x^2+\eta_y^2+\eta_z^2)^{1/2}\frac{\partial}{\partial \eta}(\rho e/\rho)/[\rho_\infty u_\infty (H_\infty - h_w)] \tag{13}$$

The coordinate transformation derivatives are included as a consequence of obtaining the heat flux normal to the body surface, $\dot{q}=\hat{n}\cdot k\nabla T$. The overall comparison between data and computational results is only fair. The peak heating is consistently concentrated around the exposed blunt leading edge of the fins and strake. Since no thermocouples could be installed at these leading edges because of their size, a verification by the analytic solution based upon the reference temperature method for the stagnation point was performed.[17] The analytic solution yielded a Stanton number of 1.243×10^{-2}, which is within 10% of the numerical prediction locally. However, the persistent and maximum discrepancy (20%) between data and the present calculations is located on the windward surface and over a wide range of the streamwise stations.[7,9] This behavior has been commonly detected in numerical simulations of flowfields with incidence. In all, the present calculations follow the trend found in experimental data in revealing the peak heating of the exposed leading edges and troughs of heat transfer on the leeward surface and corner regions between fins.

Surface pressure and the Stanton number distribution comparisons with the parabolized Navier-Stokes (PNS) solutions at their furthest downstream station ($x/r=108$) are presented in Figs. 7 and 8, respectively. The agreement in surface pressure distribution is very good. The difference in the heat-transfer data is more noticeable in the leeward surface beneath the rollup of the vortex. Better agreement is reached on the windward surface, and both numerical values underpredict the experimental measurement.

The windward and leeward pressure distributions along the plane of symmetry are given in Fig. 9. Clearly, the outstanding feature is for a hypersonic lifting configuration the

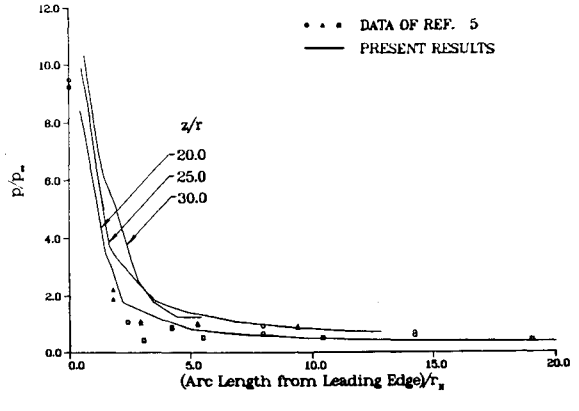

Fig. 4 Surface pressure distributions on the central fin.

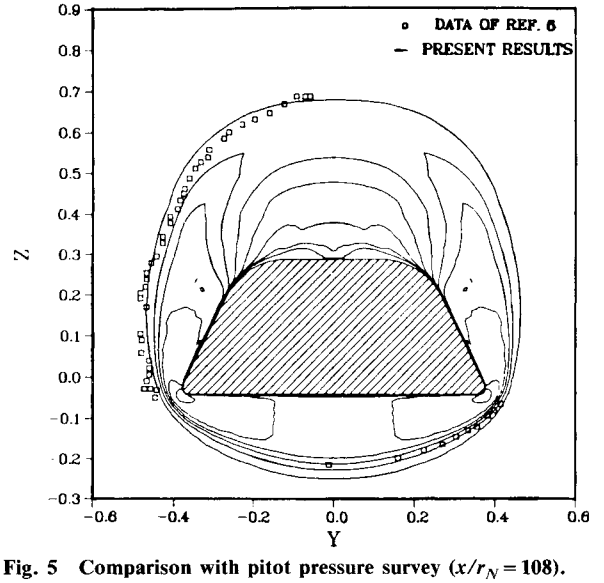

Fig. 5 Comparison with pitot pressure survey ($x/r_N=108$).

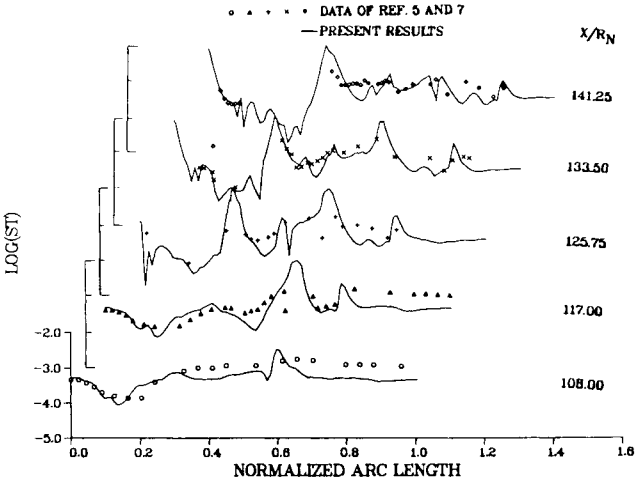

Fig. 6 Peripheral heat-transfer distributions.

Table 1 Comparison of lift and drag coefficients

	C_L	C_D	L/D
Experimental data	3.676×10^{-2}	3.173×10^{-2}	1.158
Numerical results	3.503×10^{-2}	2.960×10^{-2}	1.183
Percent error	4.71	6.71	2.16

surface pressure varies in magnitude over several orders. In the nose region, the pressure attains the maximum value of 41.8 times the freestream; the minimum value is only about 0.05 times the unperturbed value in the corners between the fins. The windward pressure distribution indicates the rapid expansion from the stagnation point and maintains a gradual compression throughout the windward surface until the expansion initiates at the trailing boattail. The leeward surface pressure undergoes expansion from the nose, recompresses over the canopy, followed by the expansion, and finally rises over the central fin. The agreement between the parabolized Navier-Stokes solution[9] and the present result is very good in the overlapped region of investigations, excepting perhaps some mild fairing which may have caused the underprediction of the pressure value over the canopy by the parabolized Navier-Stokes procedure. The overall agreement serves to validate the present effort and confirm the choice of grid spacing in the forebody region.

Postprocessing

In this section, a reconstruction of the entire flowfield around the X24C-10D research aircraft is attempted to gain understanding of the salient features of its structure. The overall surface pressure distribution and heat transfer around the aircraft are given together with the immediately adjacent surface streamline to depict the surface shear-stress pattern and identify the possible separated flow regions. However, the graphic presentation of the flowfield in the form of Mach contours is limited to a few cross sections.

The overall surface pressure on the X24C-10D experimental aircraft is depicted in a perspective view in Fig. 10. As mentioned previously, the value of surface pressure spans several decades, therefore, an artificially compressed scale (cube root value of pressure) was used to span the range of variation. As anticipated, the high-pressure regions are easily recognizable around the nose, canopy, leading edges of the strakes, and fins where the aircraft components exposed to the oncoming stream. The extensive expansion above the leeward surface downstream of the canopy is also very apparent, but the lowest pressure level is confined to the inner fin root region of the middle fin. The evidence of interference on the middle fin, originating from the strake, is reflected by the intermittent high- and low-surface pressure values over the backward-swept fin. This phenomenon is verified by the experimental data. One of the interesting revelations is that the pressure along the side surface of the fuselage is nearly constant until the afterbody contracts to form a recessed boattail where the flow expands in the downstream direction. The recompression along the plane of symmetry to realign the orientation of vortical flow above the leeward surface is also clearly indicated.

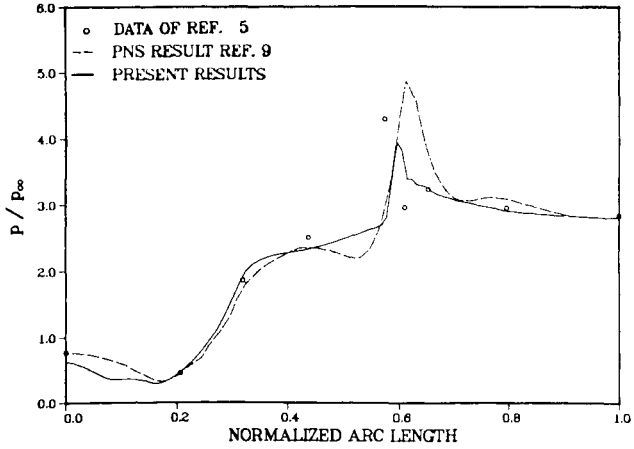

Fig. 7 Comparison of surface pressure distributions at $x/r_N = 108$.

The characteristics of heat transfer to the surface are depicted by the static temperature of the immediately adjacent nodes away from the surface, Fig. 11. Since the body surface is maintained at a constant temperature, this local temperature effectively reflects the intensity of heat transfer to the solid surface. The high heating regions generally correspond to the exposed elements of the aircraft analogous to the surface pressure. However, secondary high heating zones

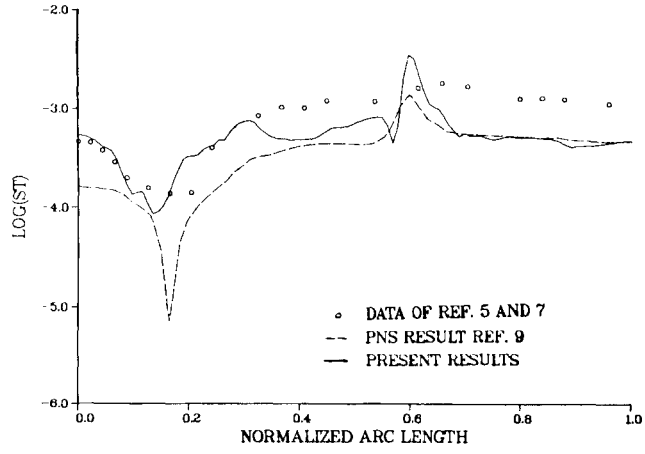

Fig. 8 Comparison of heat transfer at $x/r_N = 108$.

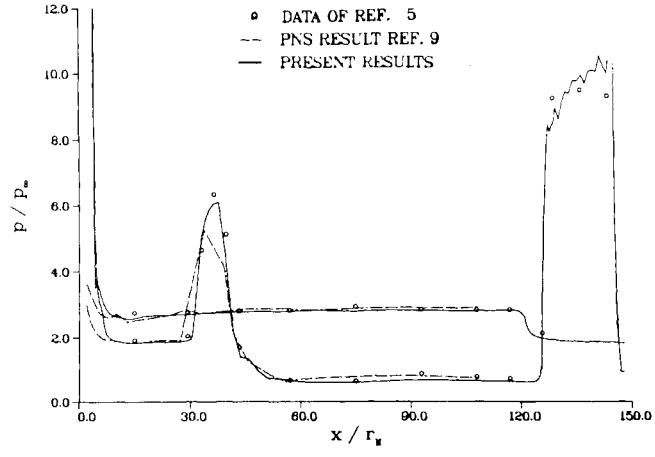

Fig. 9 Comparison of streamwise surface pressure distributions.

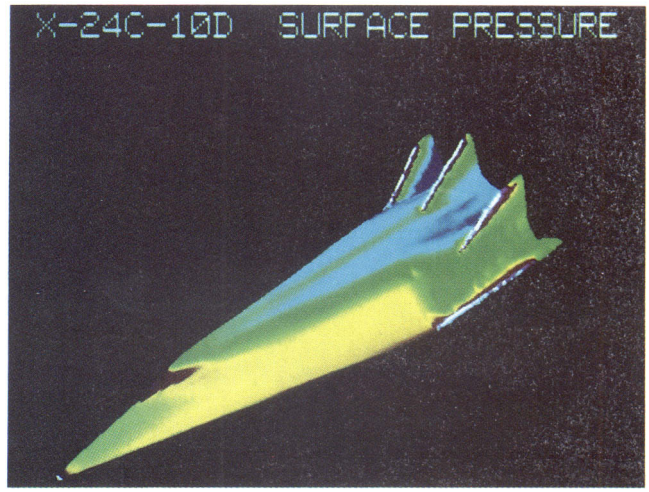

Fig. 10 Surface pressure contours.

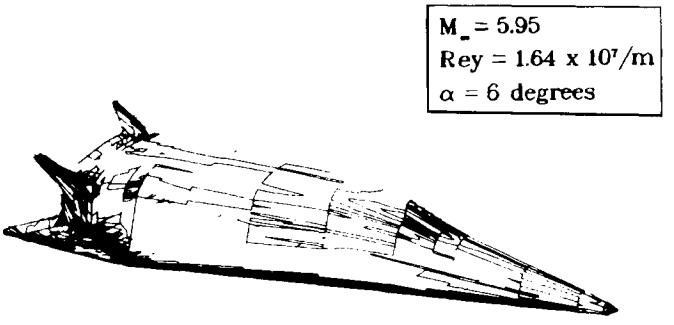

Fig. 11 Heat-transfer contours.

are also indicated in the inviscid-viscous interacting regions surrounding the canopy, adjacent to the plane of symmetry, and the areas between the strake and fins, as well as the domain bounded by the fins. The only unusual patterns observed are the overexpansion of upwash leading to a lower heat-transfer rate around the leeward outboard corner and continuing to the leading section of the strake where the afterbody recedes. All of these observations are supported by the detailed calculations presented in the previous section.

The effort involved in a complete reconstruction of the entire flowfield in a graphic presentation has proved to be prohibitive. The basic difficulty of two-dimensional projection of a three-dimensional phenomenon can, in principle, be overcome by a holographic stereogram. Unfortunately, the supporting facilities in long-haul communication and capacity of graphic work stations in simultaneous display of data still fall short. In order to exhibit the peculiar features of the

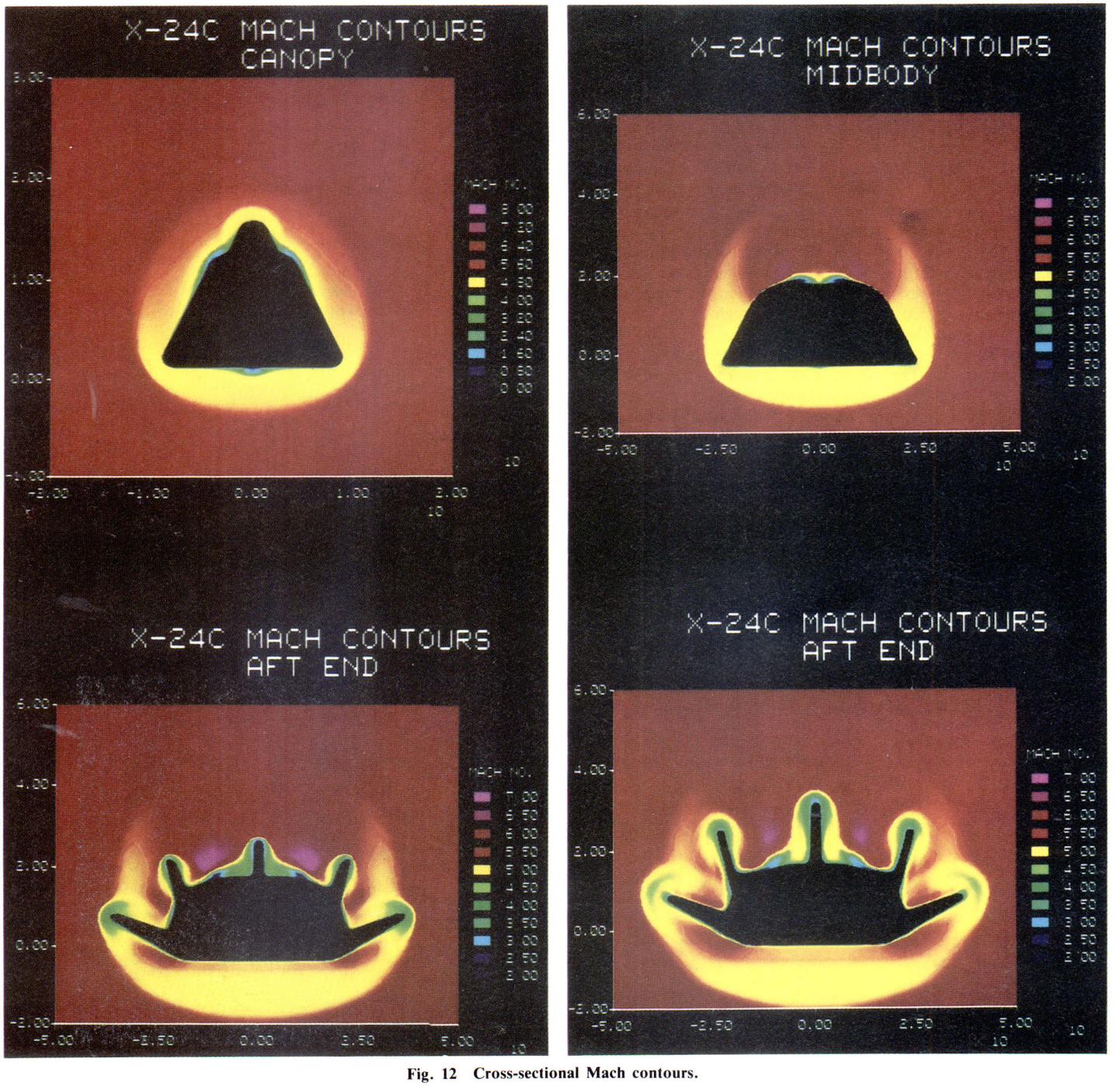

Fig. 12 Cross-sectional Mach contours.

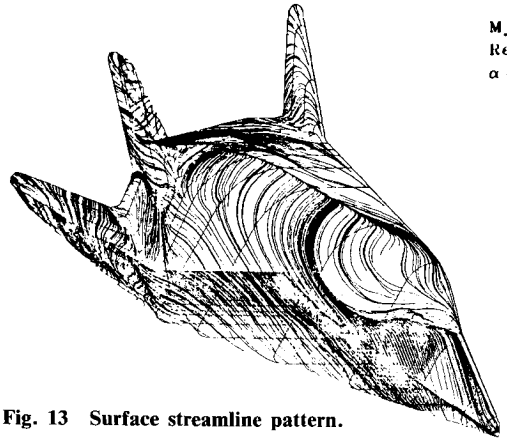

Fig. 13 Surface streamline pattern.

investigated flowfield, four cross-sectional Mach number contours are given in Fig. 12. At the streamwise station $x/r=39.5$, the induced shock-wave system over the canopy and the dispersion of the bow shock envelope over the leeward domain of this section of the forebody are apparent. At the last forebody cross section, the attenuation of the bow shock wave by the expansion from the windward to the leeward domain becomes very clear. The shock wave generated from the canopy is now completely dispersed. Similarly, the vortical formation near the leeward plane of symmetry is obvious, together with the induced higher Mach number pockets above and outboard of the vortices. At the next station downstream, $x/r=125.4$, the bow shock wave enveloping the strake impinges on the middle fin and exhibits significant distortion in structure. This interference is observed persistently over the entire afterbody even downstream of the location where the leading edge of the strake sweeps backward and parallel to the axis of symmetry of the afterbody. In the last cross-sectional plane presented, $x/r=148$, the bow shock wave originating from the blunt nose continues to exist in the windward domain. The enveloping bow shock waves over the fins and the strakes dominate the flowfield. Even though the leading edge of the strake has turned parallel to the fuselage axis, its associated bow shock wave still retains sufficient strength to interact with the bow shock wave still retains sufficient strength to interact with the bow shock waves over the middle fin. Unfortunately, little detailed information is clearly discernible by the relatively coarse supporting local mesh system. The bounding shock waves above the strakes are observed to merge with the bow shock wave generated by the blunt nose with attenuation around the lower fuselage convex corner configuration. The bow shock wave over the central fin also interacts with the vortical structure in the fin root region. However, the interaction is rather limited in intensity and is confirmed by the collapsing surface pressure distributions around the central fin (Fig. 5). It is also interesting to note that the high-Mach-number pockets induced vortically and by expansion persist even to this streamwise station.

The surface streamlines prepared by P. Buning of NASA Ames Research Center are presented in Fig. 13. This approximate surface shear flow pattern is constructed by the first node velocity components away from and parallel to the body surface. The upwash of the nose region due to the incidence and the secondary flow structure immediately upstream of the canopy are clearly revealed. The surface streamlines converging at the onset of the canopy and diverging over the canopy surface suggest a confined and small separated flow region embedded in the junction between the canopy and fuselage. The low local heat-transfer rate seems to confirm this observation. However, the crossflow separation over the leeward surface downstream of the canopy is without ambiguity. The surface streamlines also reveal tendencies to converge around the junctions of the middle fin, strake, and the afterbody implying incipient separation. The relatively low, heat-transfer distribution is in correspondence with this idea, but the topological constraints of the converging fins preclude a conclusive interpretation. An interesting observation can also be made regarding the lack of a horseshoe vortex structure around the blunt fins.[18] This may be associated with the swept-back configuration of the fins. The drastic difference in the flowfield structure between the vertical blunt fin and the swept-back fins may warrant a detailed, separate investigation.

The specific comparison of the computed drag and lift coefficients to the experimental data is presented in Table 1. The difference in lift coefficients is merely 4.72% and the drag coefficient has a discrepancy of 6.70%. However, the compensating errors in numerical underprediction yield a L/D ratio within 2.16% of the experimental measurement. This agreement is confined within the accepted experimental error band. Indirectly, this comparison seems to justify the present omission of the base drag contribution.

Conclusions

The first numerical simulation of the flowfield around a complete vehicle model, the hypersonic research aircraft X24C-10D, utilizing the Reynolds-averaged Navier-Stokes equations, has been accomplished, yielding accurate prediction of detailed flow properties. The numerical results obtained at a Mach number of 5.95 also indicate an excellent agreement in aerodynamic force coefficients with those of experimental data.

The page data structure has been demonstrated as an efficient and viable adaptation of the numerical procedure to very large class of computers without sufficient dynamic memory. The cyclic data block structure has also been found to be a convergence enhancement device by selectively processing data according to its convergence rate.

Urgent research efforts are required for continuing improvement of numerical efficiency, long-haul communication, and graphic support to enhance computational aerodynamics for aerospace vehicle design.

Acknowledgment

The authors are grateful for the computational support provided by the NASA Ames Research Center through Dr. Joseph L. Steger.

References

[1]Shang, J. S., "An Assessment of Numerical Solutions of the Navier-Stokes Equations," AIAA Paper 84-1549, 1984.

[2]Shang, J. S. and Hankey, W. L., "Numerical Solution of the Navier-Stokes Equations for a Three-Dimensional Corner," *AIAA Journal*, Vol. 15, Nov. 1977, pp. 1575–1582.

[3]Shang, J. S., Buning, P. G., Hankey, W. L., and Wirth, M. C., "Performance of a Vectorized Three-Dimensional Navier-Stokes Code on the CRAY-1 Computer," *AIAA Journal*, Vol. 18, Sept. 1980, pp. 1073–1079.

[4]Shang, J. S., "Numerical Simulation of Wing-Fuselage Aerodynamic Interaction," *AIAA Journal*, Vol. 22, Oct. 1984, pp. 1345–1353.

[5]Wannernwetsch, G. D., "Pressure Tests of the AFFDL X-24C-10D Model at Mach Numbers of 1.5, 3.0, 5.0 and 6.0," von Karman Gas Dynamics Facility, Arnold Engineering Development Center, TN, AEDC-DR-76-92, Nov. 1976.

[6]Carver, D. B., "AFFDL X24C Flowfield Survey," von Karman Gas Dynamics Facility, Arnold Engineering Development Center, TN, Project V41B-47, June 1979.

[7]Neumann, R. D., Patterson, J. L., and Sliski, N. J., "Aerodynamic Heating to the Hypersonic Research Aircraft X24C," AIAA Paper 78-37, 1978.

[8]Chaussee, D.S., Patterson, J. L., Kutler, P., Pulliam, T. H., and Steger, J. L., "A Numerical Simulation of Hypersonic Viscous Flow Over Arbitrary Geometries at High Angle of Attack," AIAA Paper 81-0050, 1981.

[9]Kaul, U. K. and Chaussee, D. S., "A Comparative Study of the Parabolized Navier-Stokes Code Using Various Grid-Generation Techniques," AIAA Paper 82-0184, 1982.

[10]Rizk, Y. M. and Ben-Shmuel, S., "Computation of the Viscous Flow Around the Shuttle Orbiter at Low Supersonic Speeds," AIAA Paper 85-0168, 1985.

[11]MacCormack, R. W., "The Effect of Viscosity in Hypervelocity Impact Cratering," AIAA Paper 69-354, 1969.

[12]Lomax, H. and Pulliam, T. H., "A Fully Implicit Code for Computing Three-Dimensional Flows on the ILLIAC IV; Parallel Computations," edited by G. Rodrique, Academic Press, New York, 1982, pp. 217-250.

[13]Baldwin, B. W. and Lomax, H., "Thin Layer Approximation and Algebraic Model for Separated Turbulent Flows," AIAA Paper 78-257, 1978.

[14]Scherr, S. J. and Shang, J. S., "Three Dimensional, Body Fitted Grid System for a Complete Aircraft," AIAA Paper 86-0428, 1986.

[15]Visbal, M. and Shang, J. S., "A Comparative Study Between an Implicit and Explicit Algorithm for Transonic Airfoils," AIAA Paper 85-0480, 1985.

[16]Newsome, R. W. Jr., "A Comparison of Euler and Navier-Stokes Solutions for Supersonic Flow Over a Conical Delta Wing," AIAA Paper 85-0111, 1985.

[17]Hayes, W. D. and Probstein, R. F., *Hypersonic Flow Theory*, Academic Press, New York, 1959, pp. 292-303.

[18]Hung, C. M. and Buning, P. G., "Simulation of Blunt-Fin Induced Shock Wave and Turbulent Boundary Layer Interaction," AIAA Paper 84-0457, 1984.

U.S. Postal Service

STATEMENT OF OWNERSHIP, MANAGEMENT AND CIRCULATION

Required by 39 U.S.C. 3685)

1A. TITLE OF PUBLICATION	1B. PUBLICATION NO.	2. DATE OF FILING
Journal of Aircraft	2 7 8 0 8 0	Oct. 27,1986
3. FREQUENCY OF ISSUE	3A. NO. OF ISSUES PUBLISHED ANNUALLY	3B. ANNUAL SUBSCRIPTION PRICE
Monthly	12	$22.00

4. COMPLETE MAILING ADDRESS OF KNOWN OFFICE OF PUBLICATION (Street, City, County, State and ZIP+4 Code) (Not printers)

1633 Broadway, New York, N.Y. 10019

5. COMPLETE MAILING ADDRESS OF THE HEADQUARTERS OF GENERAL BUSINESS OFFICES OF THE PUBLISHER (Not printer)

Same As Above

6. FULL NAMES AND COMPLETE MAILING ADDRESS OF PUBLISHER, EDITOR, AND MANAGING EDITOR (This item MUST NOT be blank)

PUBLISHER (Name and Complete Mailing Address)

American Institute of Aeronautics and Astronautics, Inc. Same As Above

EDITOR (Name and Complete Mailing Address)

Thomas M. Weeks Same As Above

MANAGING EDITOR (Name and Complete Mailing Address)

Robert Inman Same As Above

7. OWNER (If owned by a corporation, its name and address must be stated and also immediately thereunder the names and addresses of stockholders owning or holding 1 percent or more of total amount of stock. If not owned by a corporation, the names and addresses of the individual owners must be given. If owned by a partnership or other unincorporated firm, its name and address, as well as that of each individual must be given. If the publication is published by a nonprofit organization, its name and address must be stated.) (Item must be completed.)

FULL NAME	COMPLETE MAILING ADDRESS
American Institute of Aeronautics and Astronautics, Inc.	Same As Above

8. KNOWN BONDHOLDERS, MORTGAGEES, AND OTHER SECURITY HOLDERS OWNING OR HOLDING 1 PERCENT OR MORE OF TOTAL AMOUNT OF BONDS, MORTGAGES OR OTHER SECURITIES (If there are none, so state)

FULL NAME	COMPLETE MAILING ADDRESS
None	

9. FOR COMPLETION BY NONPROFIT ORGANIZATIONS AUTHORIZED TO MAIL AT SPECIAL RATES (Section 423.12 DMM only)
The purpose, function, and nonprofit status of this organization and the exempt status for Federal income tax purposes (Check one)

☑ (1) HAS NOT CHANGED DURING PRECEDING 12 MONTHS ☐ (2) HAS CHANGED DURING PRECEDING 12 MONTHS (If changed, publisher must submit explanation of change with this statement)

10. EXTENT AND NATURE OF CIRCULATION (See instructions on reverse side)	AVERAGE NO. COPIES EACH ISSUE DURING PRECEDING 12 MONTHS	ACTUAL NO. COPIES OF SINGLE ISSUE PUBLISHED NEAREST TO FILING DATE
A. TOTAL NO. COPIES (Net Press Run)	4083	4200
B. PAID AND/OR REQUESTED CIRCULATION 1. Sales through dealers and carriers, street vendors and counter sales	----	----
2. Mail Subscription (Paid and/or requested)	3567	3717
C. TOTAL PAID AND/OR REQUESTED CIRCULATION (Sum of 10B1 and 10B2)	3567	3717
D. FREE DISTRIBUTION BY MAIL, CARRIER OR OTHER MEANS SAMPLES, COMPLIMENTARY, AND OTHER FREE COPIES	73	73
E. TOTAL DISTRIBUTION (Sum of C and D)	3640	3790
F. COPIES NOT DISTRIBUTED 1. Office use, left over, unaccounted, spoiled after printing	443	410
2. Return from News Agents	----	----
G. TOTAL (Sum of E, F1 and 2 - should equal net press run shown in A)	4083	4200

11. I certify that the statements made by me above are correct and complete. SIGNATURE AND TITLE OF EDITOR, PUBLISHER, BUSINESS MANAGER, OR OWNER

Chris Troll, Controller

PS Form 3526, July 1984 (See instruction on reverse)